Geometric orbits of surface waves from a circular hydraulic jump

S. H. Hansen, S. Hørlück, D. Zauner, P. Dimon, C. Ellegaard, and S. C. Creagh*

The Center for Chaos and Turbulence Studies, The Niels Bohr Institute, Blegdamsvej 17, DK-2100 Copenhagen Ø, Denmark

(Received 23 August 1996)

We have measured the power spectra of surface waves generated by an unstable circular hydraulic jump. If the waves are scattered, the spectra show interference patterns which, using semiclassical approximations, have a simple interpretation as interfering geometric orbits. We also measure the jump radius as a function of various parameters, and find reasonable agreement with theory. [S1063-651X(97)14806-1]

PACS number(s): 47.35.+i, 03.65.Sq

I. INTRODUCTION

A circular hydraulic jump occurs when a vertical jet of liquid is directed onto a horizontal surface. The liquid spreads out in a thin layer, and then, at a certain radius, its height increases abruptly. This phenomenon has been investigated previously both theoretically [1–8] and experimentally [2–4,9–12] in a number of different contexts.

At low flow rates, the observed fluid motion is essentially stationary. This includes the position of the jump, which is circularly symmetric. At a critical flow rate, the flow becomes unstable, and although there is still a hydraulic jump, its position now fluctuates locally, breaking the circular symmetry. In particular, these fluctuations produce surface waves which radiate outwardly from the jump position. (There are certainly fluctuations inside the jump as well, but the flow there is too thin to study them properly.) If the fluctuations are not too large, then the generated surface waves are just linear capillary-gravity waves.

We have measured the power spectra of the height fluctuations in a flow on a circular plate. When the waves are free to leave the plate without scattering, we find a broadband spectrum without structure. If scattering occurs from a reflector placed in the flow, then characteristic oscillations are observed in the power spectrum. For our particular geometry, an analytic expression can be obtained, but a geometric orbit interpretation is more intuitive.

The paper is organized as follows. In Sec. II we describe the experimental apparatus used to control the flow and to measure the height fluctuations. Section III contains a description of the flow and some experimental results on the circular hydraulic jump which we compare with theory. In Sec. IV we discuss capillary-gravity waves and their properties. In Sec. V we show how to compute power spectra. In Sec. VI we analyze the measured power spectra using semiclassical approximations. Finally, we summarize in Sec. VII.

II. EXPERIMENT

A. Flow control system

A schematic of the flow control system is shown in Fig. 1.

*Present address: Division de Physique Théorique, Institut de Physique Nucléaire, Université de Paris Sud, Orsay Cedex 91406, France.

A large tank (A), containing ~150 l of deionized water, rested ~3 m above the experiment, and served as the main water reservoir. A valve (B) controlled the flow rate into the bottom of a 2-m-tall, 12-cm-diameter, transparent graduated cylinder (C). A variable height runoff spout (D) set the maximum water level in the cylinder, which was typically 150–180 cm. By adjusting the valve (B) carefully, a constant height could be maintained in the cylinder, and hence, a constant pressure at its bottom. The runoff from the spout (D) was caught by a funnel (E) (thus avoiding a direct con-
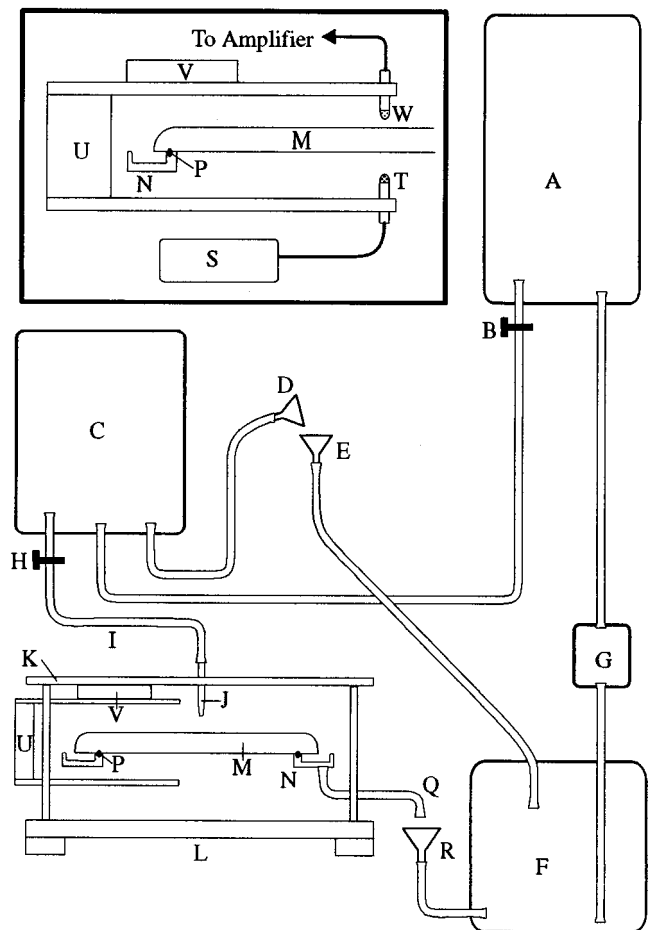

FIG. 1. The flow control system and the optical measurement system (inset) (see text).

nection) and conducted to a 120-l collection tank (F). A pump (G) then forced the water back to the reservoir (A), completing the cycle. The pump was not run during a measurement.

A second flow loop, now driven with a constant pressure, fed the experiment. A control valve (H), positioned close to the cylinder, set the flow rate into a transparent 3-m-long (to reduce entry length problems), 12-mm-diameter flexible hose (I), at the end of which was attached an 8-mm-diameter stainless steel nozzle (J). The nozzle was mounted vertically in the middle of a four-legged table (K) which rested on a heavy, vibration damped table (L). The flow from the nozzle was directed onto the center of a 2-cm-thick, 40-cm-diameter circular glass plate (M). The nozzle height was adjustable, and was fixed at 5 cm above the surface of the plate [which was itself ~25 cm above the bottom level of the cylinder (C)]. The plate rested on a circular trough (N) (shown in cross section), which had three adjustable legs (not shown) for leveling. An O ring (P) prevented water from running underneath the plate. The plate was routinely cleaned with RBS-35 detergent, otherwise the water would not uniformly wet its surface. The edge of the plate was rounded to permit a smooth runoff of the water into the trough. (The thickness of the plate was, in fact, chosen so as to give a sufficiently large radius of curvature at the edge. The reason for this will be discussed later.) A drain (Q) in the trough emptied into a funnel (R) (again avoiding a direct connection) which returned the flow back to the collection tank (F).

B. Optical system

The water height fluctuations were measured by passing a light beam through the flow and measuring the transmitted intensity. The optical system is shown in the inset to Fig. 1. An infrared laser diode (S), with a wavelength of 1550 nm, was connected to a fiber optic cable terminating in an adjustable lens (T). The lens collimated the beam to a spot of diameter $d_s \lesssim 1$ mm. The lens was mounted on the lower level of a two-tiered car (U) which could slide along a track (V) mounted underneath the table (K). The light beam was normally incident on the lower surface of the glass plate. (The plate attenuated the beam ~60% with a variation of ± 4% depending on the measuring position.) The beam was then attenuated by the water flowing on the plate, producing a transmitted intensity which varied linearly with the water height. The transmitted beam was detected with a photodiode with a fixed lens to collect refracted rays (W), mounted on the upper tier of the car. The signal from the photodiode was amplified and then processed with a Hewlett-Packard HP3562A Signal Analyzer to produce a power spectrum. The requirements to obtain a linear response and other relevant optical concerns are discussed in detail in Appendix A.

III. CIRCULAR HYDRAULIC JUMP

With the flow system described earlier, the volume flow rate Q was adjustable from 0 to 60 cm^3/s. The critical flow rate discussed in the introduction, above which the flow becomes unstable, was found to be $Q_c \approx 15$ cm^3/s. At higher flow rates $Q > 40$ cm^3/s, the flow becomes quite agitated although a jump is still discernible. The surface wave studies
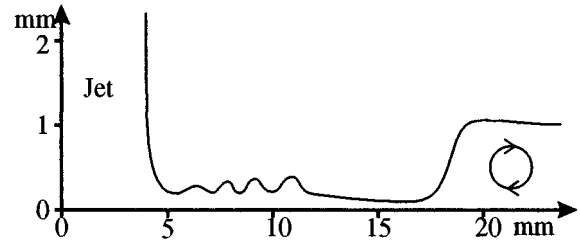

FIG. 2. A visual observation, with approximate scales, of the height profile of the flow in the stationary regime. (Note that the vertical and horizontal scales are not the same.) An eddy is observed just beyond the jump.

were all conducted at $Q = 20$ cm^3/s, where surface waves are generated but are still of small amplitude. At this flow rate, the mean jump radius was ~4.5 cm, with approximately ± 0.3-cm fluctuations.

It was difficult to determine Q_c accurately because of small disturbances (probably turbulent bursts) produced by the flow system. Initially, for example, the control valve (H) (see Fig. 1) was a precision valve with a relatively small and geometrically complicated flow chamber. When this valve was replaced with a larger and smoother (but less precise) valve, the disturbance rate decreased dramatically. We had, in fact, originally intended to study the transition from stable to unstable flow, but it became apparent that this would require a much quieter flow system which did not sacrifice precision.

Even for stationary flow ($Q < Q_c$), the profile of the water surface is rather complicated. Figure 2 shows a visual observation, with approximate scales, of the radial height profile of the flow. (In the stationary regime, the flow always has circular symmetry.) The hydraulic jump is by far the most prominent feature, but there are other structures as well. Most notably, before the jump, there is an undulating structure which increases in amplitude with radius, but ceases abruptly well before the jump. As the flow rate is increased, the amplitude of these undulations decreases, as does their wavelength, and their number increases. (The amplitude increases considerably if a little soap is added to the water, which has the effect of lowering the surface tension. This is, in fact, how these structures first came to our attention.) Furthermore, within the flow, there is an eddy, which has been observed previously [2,11]. This is easily demonstrated by dropping dye into the flow before the jump, which then becomes trapped just beyond the jump. The height after the jump is almost constant, 1–2 mm, depending on the flow rate, and only decreases, and rather abruptly, near the edge of the plate. Conservation of volume (the fluid is incompressible) requires that $Q = 2\pi r h \bar{u}$ where $\bar{u}$ is the mean flow velocity. Thus, if the height is constant, $\bar{u} \sim 1/r$. This is predicted theoretically as a possible solution for an inviscid fluid as $r \to \infty$ [8], and also by more sophisticated solutions which include viscosity [1–3,8].

The jump radius r_j was measured as a function of the flow rate by projecting a blown-up image of the flow onto a screen and simply using a ruler. The results are shown in Fig. 3 for water, and also for two oils with relative viscosities
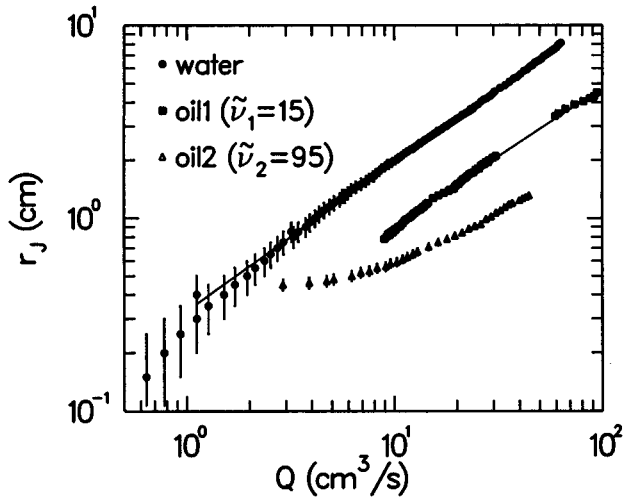
FIG. 3. Radius of the jump position as a function of the flow rate for three liquids with different relative viscosities $\widetilde{\nu} = \nu/\nu_{\text{water}}$. The solid lines are power-law fits (see text).

$(\widetilde{\nu} = \nu/\nu_{\text{water}})$ $\widetilde{\nu}_1 = 15$ and $\widetilde{\nu}_2 = 95$, respectively. (For these measurements a different plate with diameter 33 cm and thickness 4 mm was used. Also, since it was impractical to fill the entire system with oil, only the cylinder (C) in Fig. 1 was filled and then allowed to slowly drain. The flow rate was then computed from the volume rate of change.) For the water data, it should be noted that, when $Q > Q_c$, the jump radius is actually fluctuating, so what is shown is the observed mean radius. The oil data were essentially stationary at all flow rates. The water data are consistent with previous measurements [2,9,11,12]. The jump profiles are actually not sharp but have a width of several millimeters corresponding approximately to a capillary length. (The capillary length is $a = \sqrt{2\gamma/\rho g}$, where γ is the surface tension, ρ is the density, and g is the gravitational acceleration. For water, $\gamma = 74$ dyn/cm, $\rho = 1$ g/cm^3, and $g = 981$ cm/s^2, so $a = 3.9$ mm.)

At higher flow rates, it appears that $r_j \sim Q^b$ with $b \approx 0.77$ for water, and $b \approx 0.72$ for the less viscous oil. (The more viscous oil could not be measured over a wide enough range of flow rates to establish an exponent. Moreover, it was difficult to observe the jump at low flow rates, so the first few points are not reliable.) We also found only a weak dependence of the jump radius on the nozzle diameter d_n, as shown in Fig. 4. Replacing the 8-mm nozzle with a 4-mm nozzle resulted in an increase in the jump radius of only $\sim 10\%$. These results compare favorably with the prediction of Bohr, Dimon, and Putkaradze [8] that $r_j \sim Q^{5/8}\nu^{-3/8}g^{-1/8}$. They do not support the dimensional analysis argument of Godwin [7] that $r_j \sim Q^{1/3}\nu^{-1/3}d_n^{2/3}$. We were not able to determine an exponent for the viscosity in a meaningful way, but the general trend of the curves in Fig. 3 is roughly consistent with Ref. [8].

IV. SURFACE WAVES

Figure 5 shows a power spectrum of the height fluctuations with the geometry shown in Fig. 6. It was measured with a mean jump radius $x_j = 4.5$ cm, at a measuring position
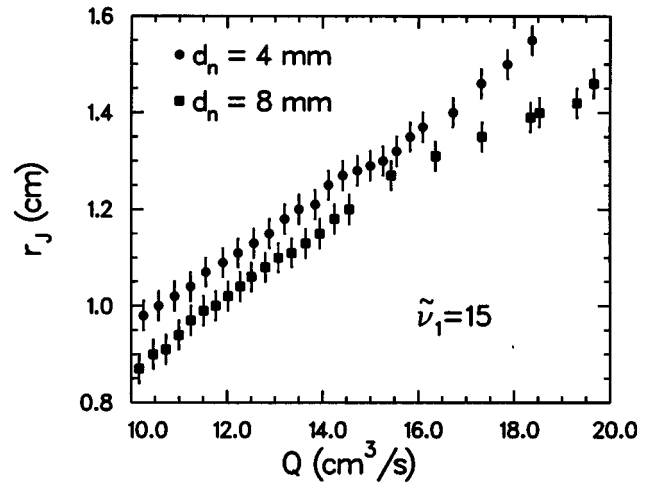

FIG. 4. Radius of the jump position vs flow rate for two different nozzle diameters.

$x = 12$ cm, and both with and without a reflector at $x_r = 16$ cm. When the reflector is inserted, an interference pattern appears. However, it should be noted that this interference is weak, and requires sufficient averaging to be observed. The data shown in Fig. 5 consist of 250 averages. (The power spectrum when $Q < Q_c$, i.e., in the stationary regime where there are no surface waves, is a factor $\sim 10^{-3}$ smaller than the spectra in Fig. 5.)

This interference phenomenon was, in fact, first observed using the 4-mm-thick glass plate and no reflector. Although the edge of the plate was rounded, the small radius of curvature (comparable to a capillary length) caused some partial reflection of the surface waves, and hence interference was unavoidable. For this reason we switched to the thicker glass plate described in Sec. IIA with its correspondingly larger radius of curvature at the edge. This plate produced no reflections from its edge, thus allowing a clean measurement of the background spectrum (i.e., with no reflector) shown in Fig. 5.
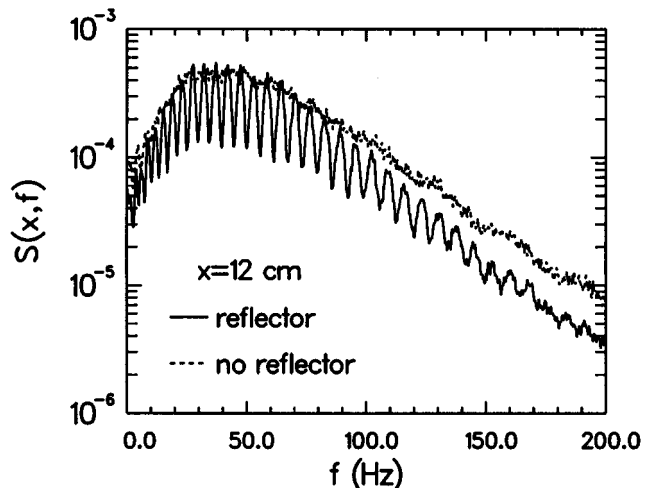

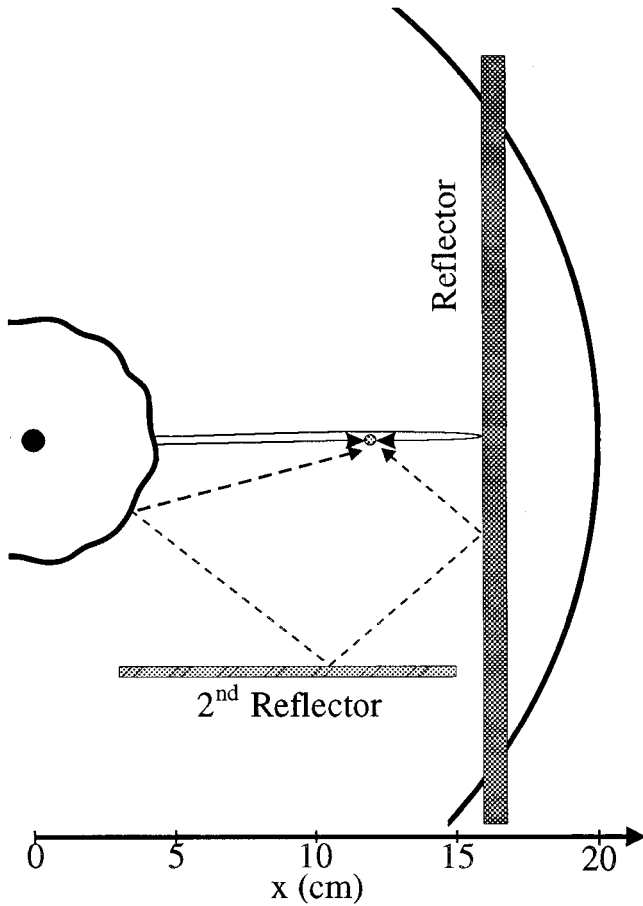FIG. 5. Power spectrum with (solid line) and without (dashed line) a reflector.

FIG. 6. The geometry on the surface of the plate. The thin lines emanating from the unstable jump show the two interfering orbits. Also shown is a second reflector, inserted later, parallel to and 8 cm away from them (see Sec. VI). The dashed lines show a new pair of interfering orbits.

In order to fully understand such spectra, we must first consider the nature of capillary-gravity waves in greater detail. To begin with, in Fig. 7 we show the different dispersion regimes for undamped capillary-gravity waves in water. Also shown are the dispersion relations for two different heights. For frequencies $f < 5$ Hz, we see that the waves are essentially shallow-water gravity waves. For $f > 30$ Hz they are essentially deep-water capillary waves. The height, therefore, is an important factor, although the dispersion relation is not very sensitive to variations in it except at rather low frequencies. For $Q = 20$ cm^3/s, the mean height (without the reflector) decreased from $h \simeq 1.5$ mm at $x = 6$ cm to $h \simeq 1.2$ mm at $x = 12$ cm, so it is actually not quite constant. When the reflector was inserted, the overall height increased to $h \simeq 1.6$ mm at $x = 6$ cm and $h \simeq 1.4$ mm at $x = 12$ cm. The rms variation from surface fluctuations was ~ 0.1 mm.

It will also be observed in Fig. 5 that the amplitude of the interference oscillations decreases with increasing frequency. This is caused both by damping (viscosity) and also by the finite size of the light beam. The smallest observable wavelength is $\lambda_{\min} \sim 2 d_s \sim 2$ mm, which corresponds to a maximum observable frequency $f_{\max} \sim 250$ Hz (see Fig. 7). The presence of damping requires that we use a dispersion relation which includes the dissipative effects of viscosity. This
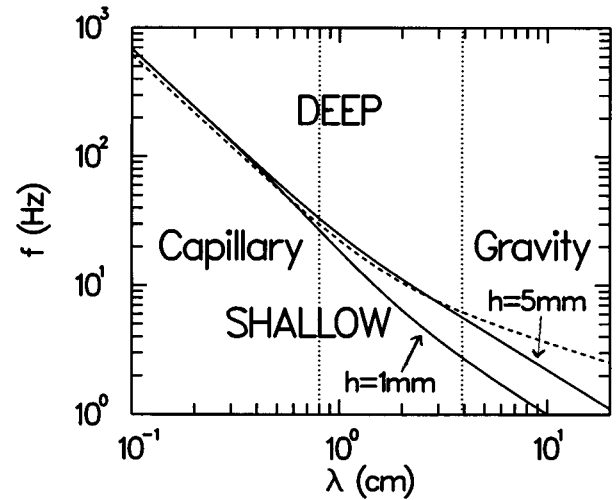

FIG. 7. Dispersion relation $f(\lambda)$ of undamped capillary-gravity waves in water. The vertical dotted lines represent the approximate boundaries for pure capillary waves (small wavelengths) and gravity waves (long wavelengths). The region in the middle has mixed capillary-gravity waves. The dashed line represents the relatively sharp boundary between the shallow- and deep-water limits. The solid lines show the dispersion relation for water with two different depths.

is computed in Appendix B. It is found that typical damping lengths are ~ 5–10 cm (see Fig. 16), which are comparable to the size of the system and so cannot be ignored.

We must also consider the frequency (doppler) shift of the surface waves caused by the flow. For a wave with radial wave vector k_0, the observed frequency will be approximately given by $\omega \simeq \omega_0 + \bar{u} k_0$ where ω_0 is the frequency in the absence of a flow. Thus we would like the phase velocity of the surface waves, $v_p = \omega_0 / k_0$, to be much smaller than the flow velocity. For the data shown in Fig. 5, the mean flow velocity at the measuring point is $\bar{u} = Q/2\pi x h \simeq 1.8$ cm/s, which exceeds 10% of v_p only for $f < 25$ Hz.

V. POWER SPECTRA

In Appendix C we compute the power spectrum for a driven dissipative linear equation with a spatially uncorrelated source term. We propose that the hydraulic jump can be modeled by such a source. The result is

$$S(\mathbf{x}, \omega) = S_f(\omega) \int |\widetilde{G}(\mathbf{x}, \mathbf{x}', \omega)|^2 \rho(\mathbf{x}') d^d x', \qquad (1)$$

where $\widetilde{G}(\mathbf{x}, \mathbf{x}', \omega)$ is the Green's function for the linear equation, $S_f(\omega)$ is the spectrum of the source, and $\rho(\mathbf{x})$ is its spatial density. We then argue that $\widetilde{G}(\mathbf{x}, \mathbf{x}', \omega)$ could be constructed from the free-wave Green's function $g_0(k|\mathbf{x} - \mathbf{x}'|)$ where $k(\omega) = k_0 + i\beta$ is the dispersion relation for damped capillary-gravity waves derived in Appendix B 2.

For simplicity, we will now consider the source (the jump) to be a point source at $\mathbf{x}_0$. Then $\rho(\mathbf{x}) = \delta(\mathbf{x} - \mathbf{x}_0)$, and Eq. (1) becomes simply

$$S(\mathbf{x},\omega)=S_f(\omega)|\widetilde{G}(\mathbf{x},\mathbf{x}_0,\omega)|^2. \qquad (2)$$

If we consider the geometry in Fig. 6, it is evident that we can obtain an analytic solution by placing an image source at $x_i=2x_r-x_j$. Then the Green's function is just the sum of the Green's functions for both source and image, and so the power spectrum along the x axis can be written as

$$S(x,\omega)=S_0(x,\omega)\left|1+be^{i\theta}\frac{g_0[k(x_i-x)]}{g_0[k(x-x_j)]}\right|^2, \qquad (3)$$

where we have inserted a factor $be^{i\theta}$ ($0\leq b\leq 1$) to account for the boundary condition at the reflector, and

$$S_0(x,\omega)=\tfrac{1}{16}S_f(\omega)|g_0[k(x-x_j)]|^2 \qquad (4)$$

is the background spectrum measured without a reflector, i.e., $b=0$. (If all the energy is reflected, then $b=1$.)

The phase θ will depend on the precise details of the boundary condition at the reflector. This is not simple for a liquid. There will be a boundary layer of width $\delta\sim\sqrt{2\nu/\omega}$ which will be unimportant if $\delta k_0\ll 1$. This is equivalent to examining the validity of the weak-damping approximation at high frequencies (see Appendix B). It is easily checked that $\delta k_0\lesssim 0.02$ over our measured frequency range, so the wave motion should be essentially an antinode at the reflector. At the contact line, however, the situation is more complicated, since the liquid can wet the surface of the reflector. Even then, the contact line can become pinned due to surface roughness. Finally, surface tension will produce a miniscus at the reflector with dimensions of the order of a capillary length. We therefore make no attempt to predict the phase since, for the above reasons, it may not even be reproducible.

In Appendix C we discuss as a specific example the telegraph equation for which the two-dimensional result is $g_0(k|\mathbf{x}-\mathbf{x}'|)=(i/4)H_0^{(1)}(k|\mathbf{x}-\mathbf{x}'|)$. At large distances, or equivalently, short wavelengths, the asymptotic form (which for our system parameters would be highly accurate above ~ 1 Hz) is then

$$g_0(k|\mathbf{x}-\mathbf{x}'|)\simeq\frac{i}{4}\left(\frac{2}{\pi k|\mathbf{x}-\mathbf{x}'|}\right)^{1/2}e^{i(k|\mathbf{x}-\mathbf{x}'|-\pi/4)}. \qquad (5)$$

If we assume that the true Green's function for capillary-gravity waves behaves similarly, then the normalized spectrum $S_N(x,\omega)=S(x,\omega)/S_0(x,\omega)$ (which is therefore independent of the source power spectrum) can be written as

$$S_N(x,\omega)=|1+\mu be^{i\theta}e^{-\beta L}e^{ik_0 L}|^2, \qquad (6)$$

where $\mu=\sqrt{(x-x_j)/(x_i-x)}$ and $L=2(x_r-x)$. We can rewrite this in the form $S_N(x,\omega)=A(\omega)+B(\omega)\cos(k_0 L+\theta)$, where $A(\omega)=1+\mu^2 b^2 e^{-2\beta L}$ and $B(\omega)=2\mu b e^{-\beta L}$ are slowly varying functions of ω, so that the interference term is explicit. (We also implicitly assume that θ varies sufficiently slowly with frequency as to be considered constant.) Note that for this particular case the argument of the interference term does not depend on the source (jump) position.

VI. SHORT-WAVELENGTH LIMIT

The calculation in Sec. V can be generalized to more complicated geometries in a straightforward way if we employ semiclassical approximations [13]. These apply in the short-wavelength limit, and express the Green's function as a sum over geometrical orbits α as

$$\widetilde{G}^{\text{sc}}(\mathbf{x},\mathbf{x}',\omega)\approx\sum_\alpha A_\alpha(\mathbf{x},\mathbf{x}',\omega)e^{i\mathcal{S}_\alpha(\mathbf{x},\mathbf{x}',\omega)}. \qquad (7)$$

Here α labels an orbit going from $\mathbf{x}'$ to $\mathbf{x}$ in the geometrical limit of the wave equation (analogous to the geometrical limit of optics, for example). In general, such an orbit is obtained by using the local dispersion relation $\omega(\mathbf{x},\mathbf{k})$ to generate classical trajectories, or rays, according to Hamilton's equations $(\dot{\mathbf{x}},\dot{\mathbf{k}})=(\partial\omega/\partial\mathbf{k},-\partial\omega/\partial\mathbf{x})$. Since in our case the dispersion relation is only weakly dependent on position, the orbits are effectively lines, but reflections can occur at boundaries to produce nontrivial interference effects. A complete analysis of this approximation as it applies to calculations of the present type is given in Ref. [14]. More general background, concentrating on the case where the wave system corresponds to the Schrödinger equation in quantum mechanics, is given in Ref. [13]. Each orbit donates to the Green's function a contribution with the accumulated phase $\mathcal{S}_\alpha(\mathbf{x},\mathbf{x}',\omega)=\int_{\mathbf{x}'}^{\mathbf{x}}\mathbf{k}\cdot d\mathbf{x}$. The amplitude $A_\alpha(\mathbf{x},\mathbf{x}',\omega)$ is obtained from the geometry of the orbit as described in Refs. [13,14]. The advantage of this formula is that it applies even when the geometry of the system does not allow the simple decomposition of Sec. V.

If we consider for a moment a single-point source, then there are only one or two orbits, depending on whether or not the reflector is in the flow. Then the semiclassical Green's function Eq. (7), becomes simply

$$\widetilde{G}^{\text{sc}}(x,x_j,\omega)\approx A_1 e^{ik_0(x-x_j)}+A_2 e^{ik_0(x-x_j)}e^{i2k_0(x_r-x)}, \qquad (8)$$

where the imaginary part of the wave vector has been absorbed in the amplitudes. The normalized form of the power spectrum, Eq. (2), can then be written as

$$S_N^{\text{sc}}(x,\omega)=|1+b'e^{i\theta}e^{ik_0 L}|^2, \qquad (9)$$

where $S_0^{\text{sc}}(x,\omega)=S_f(\omega)|A_1|^2$, $b'e^{i\theta}=A_2/A_1$, and L can now be interpreted as the difference in the orbit lengths. We note that Eq. (9) has the same form as the asymptotic result for the pedagogical analytic example, Eq. (6). However, it should be emphasized that a simple analytic expression such as Eq. (3) can only be found for our special geometry (point source, straight reflector), whereas the semiclassical method is more generally applicable.

A complication occurs in the actual system, however, in that the source is not a point but is spatially extended, presumably over the annular region occupied by the jump itself. Therefore it is necessary to integrate over the source position as in Eq. (1). Once again, this is described in detail in Ref. [14]. Here we simply cite the main effect, which is that the dominant contribution, which comes from source points for which the phase is stationary with respect to variation of the source position, corresponds in the case of a single reflector to an orbit emerging radially from the jump. The power spec-
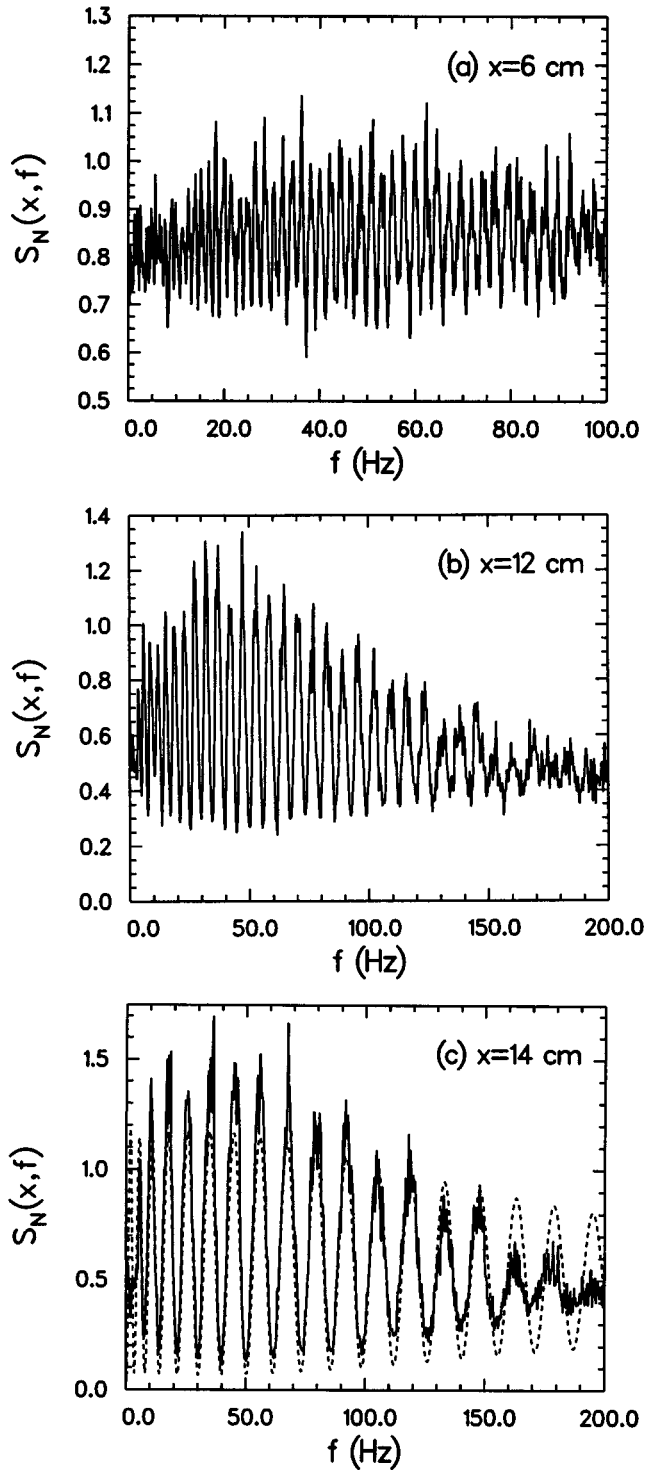
FIG. 8. Normalized power spectra for (a) $x=6$ cm, (b) $x=12$ cm, and (c) $x=14$ cm. The dashed line in (c) shows the self-consistency of the analysis (see text).

trum then still has the form Eq. (9). We will return to more complicated geometries below. First let us examine the correspondence between the prediction Eq. (9) and the actual data.

In Figs. 8(a)–8(c), we show the normalized spectra for $x=6$, 12, and 14 cm, respectively. (They do not approach unity at high frequency because, as discussed previously in Sec. IV, there is a small increase in the water height when

the reflector is inserted in the flow, which causes a small additional amount of absorption of the light beam.) It is clear now that the peaks in the interference pattern are not evenly spaced due to the nonlinear dispersion relation for capillary-gravity waves.

In order to extract the orbit length difference L, we must express the normalized spectrum as a function of k_0. Thus we must make the change of variable $f \rightarrow k_0$ using the dispersion relation calculated in Appendix B. We can then compute the Fourier transform

$$\Lambda(x,\xi) = \int S_N(x,k_0) e^{-ik_0\xi} dk_0. \tag{10}$$

The modulus of $\Lambda(x,\xi)$ for the spectra in Figs. 8(a)–8(c) is shown in Figs. 9(a)–9(c). In each case there is a strong peak whose position is just the orbit length difference L. The phase at the peak is just θ. The values for L are consistent with the actual measured values, with some small discrepancies that are probably a consequence of the messy boundary conditions at the reflector which also determine the phase (see Sec. V). The peak widths are a consequence of the finite frequency range over which the power spectrum was measured.

Inserting the values found in Fig. 9 into Eq. (6), or equivalently Eq. (9) (and taking $b=1$ and correcting for the increased light absorption with the reflector in place), we can check our analysis for self-consistency. We show an example of this as the dashed line in Fig. 8(c). (Similar results are found for the other spectra, but we do not show them for reasons of clarity.) There is more attenuation at high frequencies in the measured data than in the theory, but this is probably a consequence of the finite beam size, as discussed in Sec. IV.

If we add a second reflector as shown in Fig. 6, additional orbits appear, the topology of which is indicated by the dashed lines in the figure. The result of integrating over the source position is less simple for these orbits, because there is no source position for which the phase is stationary. A contribution will still arise, however, dominated by the limits of the integration region, but the equivalent expression for the contribution to the power spectrum is considerably more complicated and we will not go into it in detail. Figure 10 shows $|\Lambda(x,\xi)|$ for this new configuration. A new peak does indeed appear at $\xi=12.6$ cm, which is consistent with the length of orbits of the type shown in the figure. We expect more complicated orbits of this type to be a general feature of systems with closed boundary conditions. For a completely closed system the number of orbits can be dramatically larger, although the effects of longer orbits will be suppressed by the presence of dissipation.

VII. SUMMARY

We have studied the surface height fluctuations created by an unstable circular hydraulic jump. When the fluctuations are small, they are just ordinary capillary-gravity waves. If a reflector is placed in the flow, the measured power spectrum shows an interference pattern. If we treat the jump as a spatially uncorrelated broadband source, then the interference has a simple interpretation using semiclassical approxima-
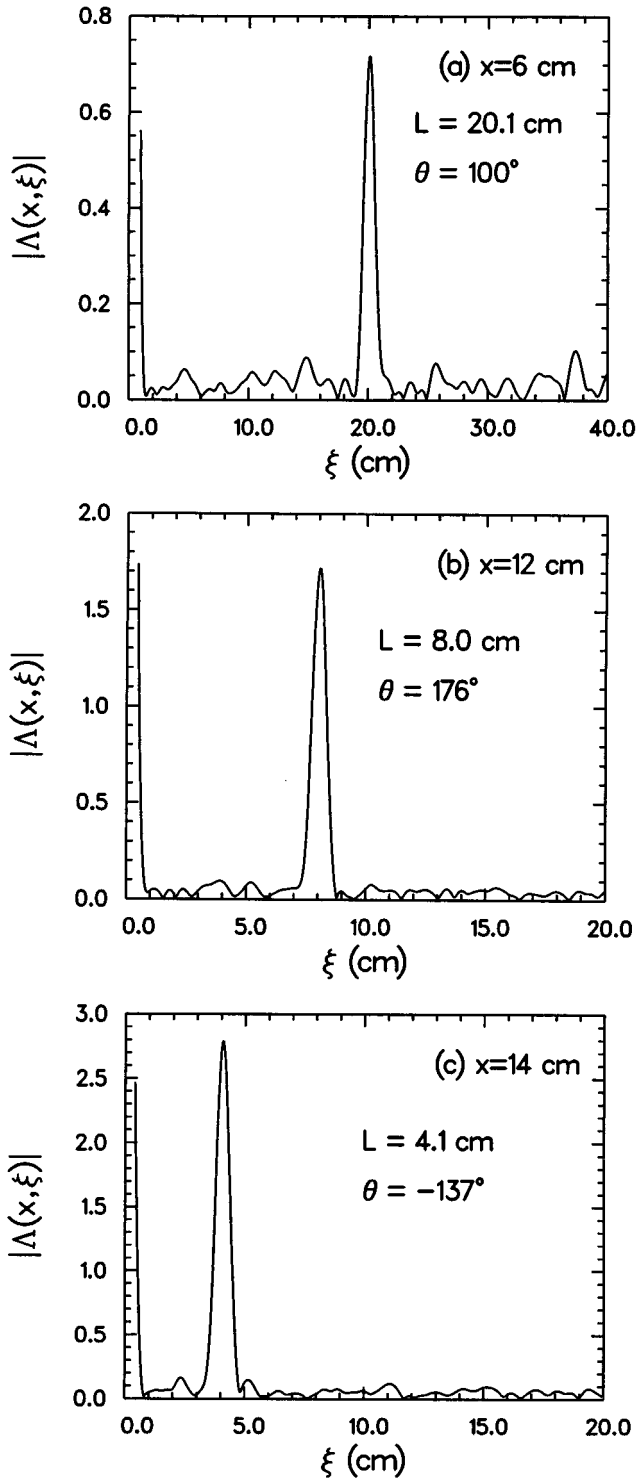
FIG. 9. Modulus of $\Lambda(x,\xi)$ for (a) $x=6$ cm, (b) $x=12$ cm, and (c) $x=14$ cm.

FIG. 10. Modulus of $\Lambda(x,\xi)$ for $x=12$ cm with a second reflector in the flow. A new peak is now visible at $\xi=12.6$ cm.

wave medium, for example. This may have possible relevance to fields such as seismology and helioseismology.

APPENDIX A: OPTICAL CONSIDERATIONS

One can think of the free surface as having two degrees of freedom at the point where the light beam passes through it: a vertical translation, and a tilt. Although we are only interested in variations in the transmitted light intensity arising from the former (attenuation), we must also consider the effects of the latter (refraction).

1. Attenuation

A measurement of the transmitted intensity I through deionized water of different heights h is shown in Fig. 11. The data follow the expected law

$$I(h)=I_0e^{-h/\ell}, \tag{A1}$$

yielding an attenuation length $\ell=0.67$ mm for a light wavelength of 1550 nm.

There are several considerations in choosing an appropriate wavelength. If the height fluctuates, then from Eq. (A1) we have

$$\delta I/I=-(\delta h/\ell)+\tfrac{1}{2}(\delta h/\ell)^2+\cdots. \tag{A2}$$

A linear response requires that the dynamic range $|\delta h/\ell|\ll1$, but, of course, it should be as large as possible by choosing the smallest ℓ for which this condition is satisfied. Physically, we expect that $|\delta h|\ll h$, but, then again, we

tions. A similar phenomenon should also appear in other systems with spatially uncorrelated broadband source spectra. For example, a microwave cavity may show such interference using its own blackbody radiation as a source. More generally, this experiment has demonstrated a mechanism whereby, even in situations where the excitations of a wave system are fundamentally stochastic in origin, it is possible to extract coherent interference effects. Such coherent effects might be used as a probe to determine the properties of the
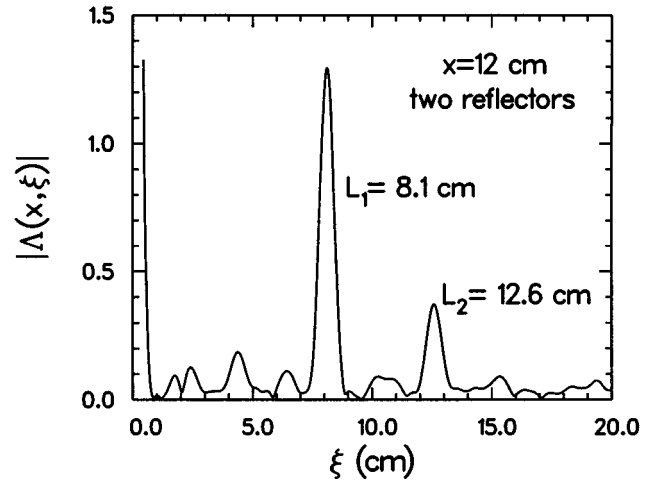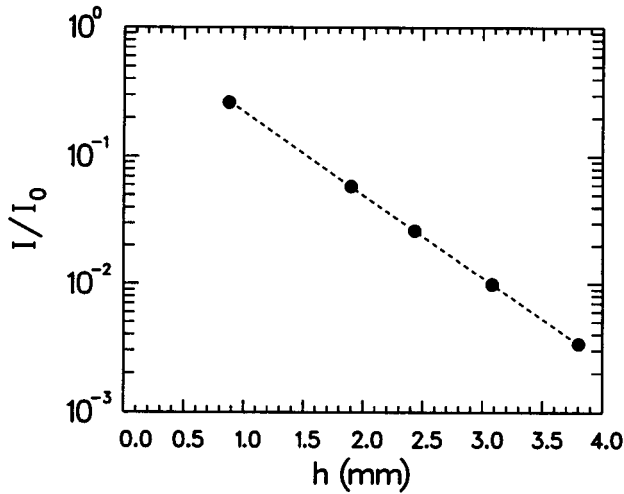
FIG. 11. Transmitted light intensity for different water heights. The dashed line is a fit to Eq. (A1).

do not want to lose too much intensity from attenuation so h should not exceed several attenuation lengths. Taken together, these conditions lead to the conclusion that it is desirable to have $\ell \sim h$. The attenuation length varies widely (1 μm to 10 m) in the infrared, so it is not difficult to find a convenient source wavelength. In our experiment the water height was typically 1–2 mm (depending on the flow rate), hence our choice of the wavelength above. The signal-to-noise ratio was better than 1000:1, so the smallest measurable height change is then $|\delta h|_{\min} \lesssim 10^{-3} \ell$, or $|\delta h|_{\min} \lesssim 1$ μm.

2. Refraction

As the light beam passes through the water-air interface, it will refract if the free surface is tilted due to surface waves. Figure 12 shows the refraction of a light ray as it passes through an interface tilted at an angle i from the horizontal. We are interested not in the angle of refraction r, but in the deflection from the incident beam direction $\chi = r - i$. Using
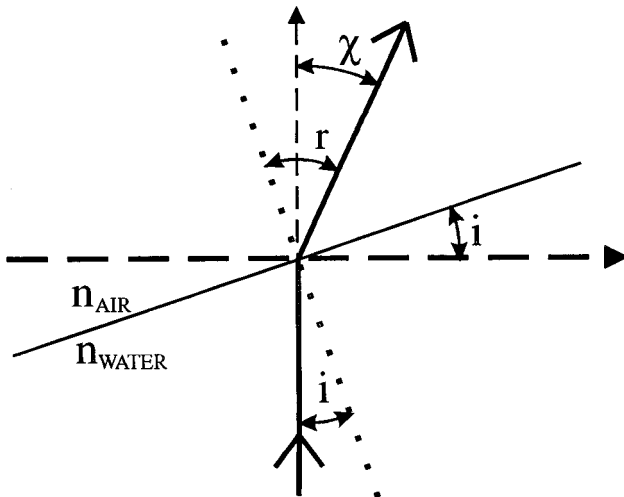

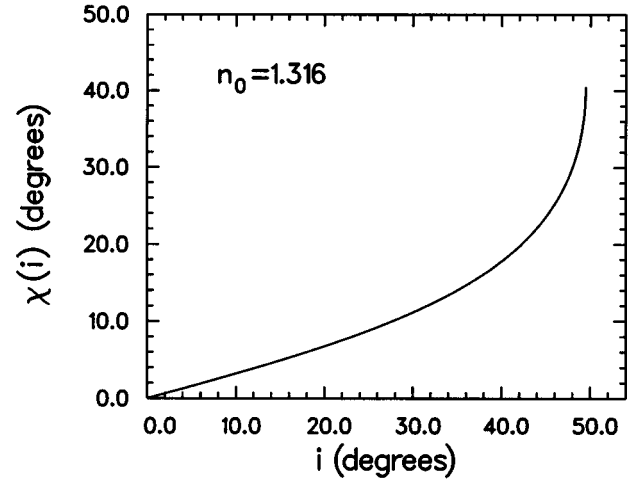FIG. 12. Geometry of the optical measurement (see text).

FIG. 13. The deflection of the incident beam as a function of the surface tilt angle.

Snell's law $\sin r = n_0 \sin i$, where $n_0 = n_{\text{water}}/n_{\text{air}}$ is the index of refraction at the interface, we find

$$\tan i = \frac{\sin\chi}{n_0 - \cos\chi}. \qquad (A3)$$

Figure 13 shows $\chi(i)$ for $n_0 = 1.316$, the index of refraction at 1500 nm. (For visible wavelengths, $n_0 = 1.33$; n_0 is only weakly dependent on wavelength in this part of the electromagnetic spectrum.) The critical angle i_c for total internal reflection occurs when $r = 90°$ and is therefore $i_c = \sin^{-1}(1/n_0) \simeq 49°$. Then, $\chi(i_c) = 90° - i_c \simeq 41°$, which is the point where the curve in Fig. 13 terminates.

Since we must capture the outgoing ray, it is clear from Fig. 13 that we must keep the tilt angle as small as possible, certainly below 40°, where χ begins to increase rapidly. It was therefore necessary to put a lens in front of the photodiode. The lens had a diameter of 1.5 cm, and was located 1.8 cm from the surface of the glass plate. Assuming that only the central 1 cm of the lens is active, and that there is at least 1 mm of water on the plate, the maximum detectable deflection angle is $\chi_{\max} = \tan^{-1}(0.5/1.7) \simeq 16°$. This corresponds to a maximum allowable tilt angle of $i_{\max} \simeq 38°$, beyond which a refracted beam will miss the active part of the lens.

This limitation puts a constraint on the maximum amplitude of a surface wave. Suppose there is a surface wave of the form $\varphi(x,t) = A\sin(kx - \omega t)$. Its peak tilt angle i_p is then

$$\tan i_p = \max|\partial\varphi/\partial x| = Ak = 2\pi A/\lambda. \qquad (A4)$$

The beam diameter d_s limits the smallest measurable surface wavelength, i.e., $\lambda_{\min} \sim 2d_s \sim 2$ mm. For this wavelength (which represents the worst case), we require that $i_p < i_{\max}$, or therefore that $A < (\lambda_{\min}/2\pi)\tan i_{\max} \approx 0.3$ mm.

The measured signal is, of course, a superposition of many surface waves. However, using Eq. (A1) to calibrate the photodiode output, we find that the rms height variation is $\langle[\delta h(x,t)]^2\rangle^{1/2} \sim 0.1$ mm. Taking this as the amplitude of a single wave, and using Eq. (A4), this corresponds to
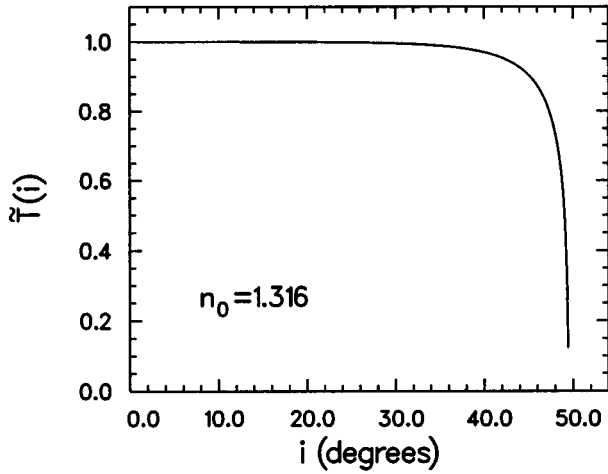
FIG. 14. The normalized transmission coefficient as a function of the surface tilt angle.

$i_p \simeq 17°$ and $\chi(i_p) \simeq 6°$, both well within the limits determined earlier. In fact, by simply monitoring the photodiode output, it was observed that the beam never left the active area of the lens, except at the highest flow rates which produced extremely large (and certainly nonlinear) surface fluctuations. Furthermore, we see that the linearity condition discussed in the first part of this appendix, which required that $\langle[\delta h(x,t)]^2\rangle^{1/2} \ll \ell$, is then also marginally satisfied.

Finally, as a surface wave passes, the initial beam intensity I_0 in Eq. (A1) will also vary in time since the reflectivity of the interface will also depend on the tilt angle. Thus Eq. (A1) should be modified to read

$$I(h,i) = I_0 \widetilde{T}(i) e^{-h/\ell}, \qquad (A5)$$

where $\widetilde{T}(i)$ is the normalized transmission coefficient such that $\widetilde{T}(0) = 1$. For an unpolarized beam (the fiber optic cable does not preserve the polarized light emitted from the laser diode), and for equal permeabilities in both media, this will have the form $\widetilde{T}(i) = T(i)/T(0)$, where [15]

$$T(i) = 1 - \frac{1}{2}\left[\frac{\sin^2(i-r)}{\sin^2(i+r)} + \frac{\tan^2(i-r)}{\tan^2(i+r)}\right], \qquad (A6)$$

and $T(0) = 4n_0/(n_0+1)^2$ is the transmitted intensity at normal incidence. (We ignore multiple reflections from the other surfaces in the experiment.) As shown in Fig. 14, $\widetilde{T}(i)$ is essentially unity up to $\sim 30°$. In fact, for small i, it is found that $\widetilde{T}(i) \simeq 1 - ai^4$, where $a = (n_0-1)^2(-n_0^2+4n_0-1)/8 \simeq 0.032$ for $n_0 = 1.316$. Thus for a single mode (and small tilt angles), $i^4 \simeq (\partial\varphi/\partial x)^4 = A^4 k^4 \sin^4(kx-\omega t)$, so the effect of this term would be to produce negligible harmonic contamination at 2ω and 4ω.

APPENDIX B: DISPERSION RELATIONS

1. $\omega(k)$ for damped capillary-gravity waves

We would like to calculate the dispersion relation for small-amplitude capillary-gravity waves on the surface of an incompressible viscous liquid of finite depth h [16]. For ease

of calculation, we will work in Cartesian coordinates, and consider a plane wave propagating in the $\hat{\mathbf{x}}$ direction in a gravitational field $\mathbf{g} = -g\hat{\mathbf{z}}$. The unperturbed surface is taken to be at $z=0$. The linearized Navier-Stokes equations are then

$$\frac{\partial v_x}{\partial t} = \nu\left(\frac{\partial^2 v_x}{\partial x^2} + \frac{\partial^2 v_x}{\partial z^2}\right) - \frac{1}{\rho}\frac{\partial P}{\partial x}, \qquad (B1a)$$

$$\frac{\partial v_z}{\partial t} = \nu\left(\frac{\partial^2 v_z}{\partial x^2} + \frac{\partial^2 v_z}{\partial z^2}\right) - \frac{1}{\rho}\frac{\partial P}{\partial z} - g, \qquad (B1b)$$

with the continuity condition

$$\frac{\partial v_x}{\partial x} + \frac{\partial v_z}{\partial z} = 0. \qquad (B1c)$$

If we assume a solution of the forms

$$v_x = \widetilde{v}_x e^{\beta z} e^{i(kx-\omega t)}, \qquad (B2a)$$

$$v_z = \widetilde{v}_z e^{\beta z} e^{i(kx-\omega t)}, \qquad (B2b)$$

$$P/\rho = \widetilde{p} e^{\beta z} e^{i(kx-\omega t)} - gz, \qquad (B2c)$$

then substitution into Eqs. (B1) requires that

$$\begin{pmatrix} -i\omega + \nu(k^2-\beta^2) & 0 & ik \\ 0 & -i\omega + \nu(k^2-\beta^2) & \beta \\ ik & \beta & 0, \end{pmatrix} \begin{pmatrix} \widetilde{v}_x \\ \widetilde{v}_z \\ \widetilde{p} \end{pmatrix} = 0,$$
$$(B3)$$

which in turn only has a solution if the determinant of the matrix vanishes. Thus we find the four solutions $\beta = \pm k, \pm\sqrt{k^2 - i\omega/\nu}$. Solving for the eigenvectors, we can write

$$v_x = [Ae^{kz} + Be^{-kz} + Ce^{mz} + De^{-mz}]e^{i(kx-\omega t)}, \quad (B4a)$$

$$v_z = (-i)[Ae^{kz} - Be^{-kz} + C(k/m)e^{mz} - D(k/m)e^{-mz}]e^{i(kx-\omega t)}, \qquad (B4b)$$

$$P/\rho = (\omega/k)[Ae^{kz} + Be^{-kz}]e^{i(kx-\omega t)} - gz, \quad (B4c)$$

where $m = \sqrt{k^2 - i\omega/\nu}$ and A, B, C, and D will be determined by the boundary conditions.

The first two boundary conditions are found from the requirement that the velocity field vanish at the bottom (fixed) surface, i.e., $v_x(x,-h) = v_z(x,-h) = 0$. This immediately gives us the two relations

$$Ae^{-kh} + Be^{kh} + Ce^{-mh} + De^{mh} = 0, \qquad (B5a)$$

$$Ae^{-kh} - Be^{kh} + C(k/m)e^{-mh} - D(k/m)e^{mh} = 0. \qquad (B5b)$$

The remaining two boundary conditions are found by balancing the forces at the free surface. The perturbed free surface

is defined by its displacement from equilibrium $\varphi(x,t)$ which is related to the velocity field by

$$\frac{\partial \varphi}{\partial t} = v_z(x,\varphi) - v_x(x,\varphi)\,\frac{\partial \varphi}{\partial x} \simeq v_z(x,\varphi), \qquad \text{(B6)}$$

where the last approximation can be made if $\partial\varphi/\partial x$ is a small quantity. This will be true if $\varphi \ll \lambda$ where λ is the wavelength of a surface wave. In this case, $\varphi(x,t)$ will have the same dispersion relation as the velocity field. If the surface is curved, the surface tension will produce a capillary force which must then balance the difference in the viscous stress forces. The viscous stress tensor in Cartesian coordinates x_i is

$$\sigma_{ik} = -P\delta_{ik} + \eta\left(\frac{\partial v_i}{\partial x_k} + \frac{\partial v_k}{\partial x_i}\right). \qquad \text{(B7)}$$

The condition at the surface is then

$$n_k(\sigma_{2,ik} - \sigma_{1,ik})_{z=\varphi} = \frac{\gamma}{R}n_i, \qquad \text{(B8)}$$

where $\sigma_{\alpha,ik}$ is the viscous stress tensor for the liquid ($\alpha = 1$) and the air above it ($\alpha = 2$), γ is the surface tension, R is the radius of curvature, and n_i is the unit vector normal to the surface. Repetition of indices implies summation. Again, for small-amplitude waves, $|n_x/n_z| = |\partial\varphi/\partial x| \ll 1$, so Eq. (B8) simplifies to

$$(\sigma_{2,xz} - \sigma_{1,xz})_{z=\varphi} \simeq 0, \qquad \text{(B9a)}$$

$$(\sigma_{2,zz} - \sigma_{1,zz})_{z=\varphi} \simeq -\gamma\frac{\partial^2\varphi}{\partial x^2}. \qquad \text{(B9b)}$$

Since $\eta_2 \ll \eta_1$, the coupling between the two fluids will be weak, and we can consider the air to be stationary. Then $\sigma_{2,ik}|_{z=\varphi} = -P_0\delta_{ik}$, where P_0 is the (constant) air pressure

at the surface. We then expand Eqs. (B9) for small φ, and keep only the lowest order (φ^0) terms. Then Eq. (B9a) becomes simply

$$\sigma_{1,xz}|_{z=0} = \eta_1\left(\frac{\partial v_x}{\partial z} + \frac{\partial v_z}{\partial x}\right)_{z=0} = 0, \qquad \text{(B10)}$$

which leads directly to the third boundary condition

$$A - B + C\left(\frac{k^2+m^2}{2km}\right) - D\left(\frac{k^2+m^2}{2km}\right) = 0. \qquad \text{(B11)}$$

The second surface boundary condition Eq. (B9b) is now

$$-P_0 + \left(P - 2\eta_1\frac{\partial v_z}{\partial z}\right)_{z=\varphi} = -\gamma\frac{\partial^2\varphi}{\partial x^2}. \qquad \text{(B12)}$$

Taking the time derivative of both sides, and using Eq. (B6), we obtain

$$\left(\frac{\partial P}{\partial t} - 2\eta_1\frac{\partial^2 v_z}{\partial z\,\partial t}\right)_{z=\varphi} = -\gamma\frac{\partial^2 v_z}{\partial x^2}. \qquad \text{(B13)}$$

Finally, using Eqs. (B4), and setting $\varphi = 0$ in the end, we arrive at the fourth boundary condition

$$A\left(1 - \frac{\omega_\infty^2}{\omega^2} + 2i\epsilon\right) + B\left(1 + \frac{\omega_\infty^2}{\omega^2} + 2i\epsilon\right) + C\left(-\frac{k\omega_\infty^2}{m\omega^2} + 2i\epsilon\right)$$
$$+ D\left(\frac{k\omega_\infty^2}{m\omega^2} + 2i\epsilon\right) = 0, \qquad \text{(B14)}$$

where $\epsilon = \nu k^2/\omega$, $\nu = \eta_1/\rho$, and $\omega_\infty^2 = gk + (\gamma/\rho)k^3$, which is the familiar dispersion relation for deep-water (i.e., infinite depth) capillary-gravity waves.

The four boundary conditions Eqs. (B5), (B11), and (B14) will only have a solution if

$$\begin{vmatrix} e^{-kh} & e^{kh} & e^{-mh} & e^{mh} \\[2mm] e^{-kh} & -e^{kh} & \dfrac{k}{m}e^{-mh} & -\dfrac{k}{m}e^{mh} \\[3mm] 1 & -1 & \dfrac{k^2+m^2}{2km} & -\dfrac{k^2+m^2}{2km} \\[3mm] 1 - \dfrac{\omega_\infty^2}{\omega^2} + 2i\epsilon & 1 + \dfrac{\omega_\infty^2}{\omega^2} + 2i\epsilon & -\dfrac{k\omega_\infty^2}{m\omega^2} + 2i\epsilon & \dfrac{k\omega_\infty^2}{m\omega^2} + 2i\epsilon \end{vmatrix} = 0. \qquad \text{(B15)}$$

The dispersion relation we seek, namely, $\omega(k)$, is implicit in this determinant. After some suitable combinations of rows and columns, it can be conveniently expressed as

$$a(1+6a^2+a^4)\tanh kh\ \tanh(kh/a)+b(1-a^2)^2$$
$$\times[\tanh kh-a\ \tanh(kh/a)]-(1+2a^2+5a^4)$$
$$+4a^2(1+a^2)\text{sech}\ kh\ \text{sech}(kh/a)=0, \quad \text{(B16)}$$

where $a=k/m$, $b=\omega_\infty^2/\omega^2$, and where we have used the identity $i\epsilon=a^2/(1-a^2)$ [17].

We will now make the weak-damping approximation, namely, that $\epsilon \ll 1$, or equivalently, $|a| \ll 1$. First, we drop exponentially small terms in Eq. (B16), and write it as a power series in a:

$$a^0[b\ \tanh kh-1]+a^1[\tanh kh-b]-2a^2[b\ \tanh kh+1]$$
$$+2a^3[3\ \tanh kh+b]+a^4[b\ \tanh kh-5]$$
$$+a^5[\tanh kh-b]=0. \quad \text{(B17)}$$

Then expressing a in terms of ϵ and expanding in powers of ϵ, we obtain

$$\omega^2=\omega_\infty^2\tanh kh\left[1-(i\epsilon)^{1/2}\frac{2}{\sinh 2kh}-(i\epsilon)\left(4+\frac{1}{\cosh^2kh}\right)\right.$$
$$\left.+O\{(i\epsilon)^{3/2}\}\right]. \quad \text{(B18)}$$

We are not finished, however, since ϵ depends on ω. Solving recursively, we arrive at the final result, to $O(\epsilon_h)$,

$$\omega=\omega_h\left[1-(i\epsilon_h)^{1/2}\frac{1}{\sinh 2kh}-(i\epsilon_h)\left(2+\frac{1}{2\cosh^2kh}\right.\right.$$
$$\left.\left.+\frac{1}{\sinh^2 2kh}\right)\right], \quad \text{(B19)}$$

where $\epsilon_h=\nu k^2/\omega_h$, and $\omega_h^2=\omega_\infty^2\tanh kh$ which is the well-known dispersion relation for capillary-gravity waves in the absence of viscosity. The $\epsilon_h^{1/2}$ term confirms the result argued for by Lighthill [18] on physical grounds. It should be observed, however, that this term vanishes in the deep-water ($h\to\infty$) limit, which is why it is necessary to retain the next order term also which does not vanish.

It should also be pointed out that Eq. (B19) is really an expansion in the variable $(i\epsilon_h)^{1/2}/\sinh 2kh$, that is, the height also plays an important role in the dissipation. For extremely shallow water, the expansion will break down, and the damping can no longer be considered weak. To consider this limit, we must return to Eq. (B16) and expand it first in powers of kh. To lowest order, it is found that $\omega=-i\omega_\infty^2 kh^3/3\nu$, i.e., the waves are overdamped. (In particular, it should be noted that for gravity waves $\omega=-igk^2h^3/3\nu$, i.e., they are purely diffusive with diffusion constant $D_0=gh^3/3\nu$.)

2. Damping coefficients

Above, we found a dispersion relation of the form

$$\omega=\omega_h(k)[1-\lambda a_1(k)-\lambda^2 a_2(k)] \quad \text{(B20)}$$

where λ is a small parameter which later will be set to unity. We now expand ω and k as follows:

$$\omega=\omega_0+\lambda\alpha_1+\lambda^2\alpha_2+\cdots,$$
$$k=k_0+\lambda\beta_1+\lambda^2\beta_2+\cdots,$$

such that ω_0 and k_0 are real. Substituting these into Eq. (B20), we find the following relations for each order of λ up to $O(\lambda^2)$:

$$\lambda^0: \quad \omega_0=\omega_h(k_0), \quad \text{(B21a)}$$

$$\lambda^1: \quad \alpha_1=-\omega_0 a_1(k_0)+\beta_1\frac{d\omega_0}{dk_0}, \quad \text{(B21b)}$$

$$\lambda^2: \quad \alpha_2=-\omega_0 a_2(k_0)-\beta_1\frac{d}{dk_0}[\omega_0 a_1(k_0)]+\beta_2\frac{d\omega_0}{dk_0}$$
$$+\frac{\beta_1^2}{2}\frac{d^2\omega_0}{dk_0^2}. \quad \text{(B21c)}$$

We will take k_0 to be the independent variable, so we can choose β_1 and β_2 to be purely imaginary, i.e., $\beta_{1,2}=i\beta_{1,2}^I$. This leaves us with seven variables and only five equations, so we must add two conditions based on physical considerations.

a. Temporal damping

If the system is driven spatially and then allowed to decay in time, then k must be real, which requires that $\beta_1^I=\beta_2^I=0$. In this case, Eqs. (B21b) and (B21c) reduce to

$$\alpha_1=-\omega_0 a_1, \quad \text{(B22a)}$$

$$\alpha_2=-\omega_0 a_2, \quad \text{(B22b)}$$

the real and imaginary parts of which yield the frequency shift Δ_α and the temporal damping coefficient α, respectively, when we set $\lambda=1$:

$$\Delta_\alpha=\text{Re}(\lambda\alpha_1+\lambda^2\alpha_2),=-\omega_0\text{Re}(a_1+a_2), \quad \text{(B23a)}$$

$$\alpha=\text{Im}(\lambda\alpha_1+\lambda^2\alpha_2)=-\omega_0\text{Im}(a_1+a_2). \quad \text{(B23b)}$$

Specifically, from Eq. (B19) we have that

$$a_1(k_0)=(i\epsilon_0)^{1/2}/\sinh 2k_0h, \quad \text{(B24a)}$$

$$a_2(k_0)=(i\epsilon_0)(2+1/2\cosh^2k_0h+1/\sinh^2 2k_0h), \quad \text{(B24b)}$$

where $\epsilon_0=\nu k_0^2/\omega_0$, and so we easily find that

$$\Delta_\alpha=-\omega_0\left(\frac{\epsilon_0}{2}\right)^{1/2}\frac{1}{\sinh 2k_0h}, \quad \text{(B25a)}$$

$$\alpha=-\omega_0\left[\left(\frac{\epsilon_0}{2}\right)^{1/2}\frac{1}{\sinh 2k_0h}+\left(\frac{\epsilon_0}{2}\right)\left(4+\frac{1}{\cosh^2k_0h}\right.\right.$$
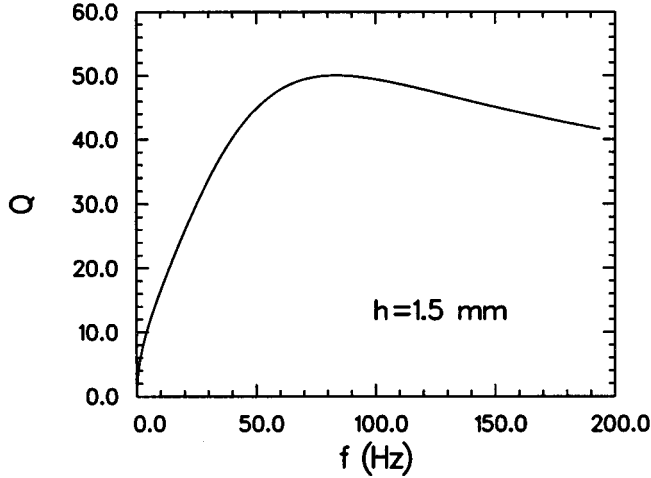$$\left.\left.+\frac{2}{\sinh^2 2k_0h}\right)\right]. \quad \text{(B25b)}$$

FIG. 15. Q as a function of frequency for water.

Note that in the deep-water ($h \to \infty$) limit, the $\epsilon_0^{1/2}$ term vanishes, as mentioned earlier, and the ϵ_0 term yields $\alpha \to -2\omega_0\epsilon_0 = -2\nu k_0^2$, the well-known result for the weak-damping limit [16].

We show in Fig. 15 the Q factor, defined as $Q = \omega_0/2\alpha$, as a function of frequency $f = \mathrm{Re}\,\omega/2\pi$, for water with depth $h = 1.5$ mm. Since the weak-damping approximation is accurate to better than $\sim 10\%$ for $Q > 5$, this figure tells us that it is valid above $f \sim 1$ Hz and up to $f \sim 100$ kHz (not shown). As discussed at the end of Appendix B 1, the Q factor becomes small at low frequency due to the excess damping encountered in the extreme shallow-water limit.

b. Spatial damping

If the system is driven temporally, and only decays spatially, then ω is real which requires that α_1 and α_2 also be real. In this case, Eqs. (B21b) and (B21c) yield the four equations

$$\alpha_1 = -\omega_0 \mathrm{Re}\,a_1, \tag{B26a}$$

$$0 = -\omega_0 \mathrm{Im}\,a_1 + \beta_1^I \frac{d\omega_0}{dk_0}, \tag{B26b}$$

$$\alpha_2 = -\omega_0 \mathrm{Re}\,a_2 + \beta_1^I \mathrm{Im}\frac{d}{dk_0}(\omega_0 a_1) - \frac{(\beta_1^I)^2}{2}\frac{d^2\omega_0}{dk_0^2}, \tag{B26c}$$

$$0 = -\omega_0 \mathrm{Im}\,a_2 - \beta_1^I \mathrm{Re}\frac{d}{dk_0}(\omega_0 a_1) + \beta_2^I \frac{d\omega_0}{dk_0}. \tag{B26d}$$

The solution gives the frequency shift Δ_β and the spatial damping coefficient β:

$$\Delta_\beta = \lambda\alpha_1 + \lambda^2\alpha_2$$

$$= -\omega_0\left[\mathrm{Re}(a_1 + a_2) - \left(\frac{\omega_0}{\frac{d\omega_0}{dk_0}}\right)\mathrm{Im}\,a_1 \mathrm{Im}\frac{da_1}{dk_0} \right.$$

$$\left. + \left\{ \frac{\omega_0}{2}\frac{d^2\omega_0}{dk_0^2}\Big/\left(\frac{d\omega_0}{dk_0}\right)^2 - 1 \right\}(\mathrm{Im}\,a_1)^2 \right], \tag{B27a}$$

$$\beta = \lambda\beta_1^I + \lambda^2\beta_2^I$$

$$= \left(\frac{\omega_0}{\frac{d\omega_0}{dk_0}}\right)\left[\mathrm{Im}(a_1 + a_2) + \mathrm{Im}\,a_1\mathrm{Re}\,a_1 \right.$$

$$\left. + \left(\frac{\omega_0}{\frac{d\omega_0}{dk_0}}\right)\mathrm{Im}\,a_1\mathrm{Re}\frac{da_1}{dk_0} \right]. \tag{B27b}$$

Again, using Eqs. (B24), we find that

$$\Delta_\beta = -\omega_0\left[\left(\frac{\epsilon_0}{2}\right)^{1/2}\frac{1}{\sinh 2k_0 h} + \left(\frac{\epsilon_0}{2}\right)\frac{f_1(k_0)}{\sinh^2 2k_0 h} \right], \tag{B28a}$$

$$\beta = \left(\frac{\omega_0}{\frac{d\omega_0}{dk_0}}\right)\left[\left(\frac{\epsilon_0}{2}\right)^{1/2}\frac{1}{\sinh 2k_0 h} + \left(\frac{\epsilon_0}{2}\right)\left(4 + \frac{1}{\cosh^2 k_0 h}\right.\right.$$

$$\left.\left. + \frac{f_2(k_0)}{\sinh^2 2k_0 h}\right) \right], \tag{B28b}$$

where

$$f_1(k_0) = -\frac{1}{2} - \left(\frac{\omega_0}{k_0}\Big/\frac{d\omega_0}{dk_0}\right)\left(1 - \frac{2k_0 h}{\tanh 2k_0 h}\right)$$

$$+ \frac{\omega_0}{2}\frac{d^2\omega_0}{dk_0^2}\Big/\left(\frac{d\omega_0}{dk_0}\right)^2, \tag{B28c}$$

$$f_2(k_0) = \frac{5}{2} + \left(\frac{\omega_0}{k_0}\Big/\frac{d\omega_0}{dk_0}\right)\left(1 - \frac{2k_0 h}{\tanh 2k_0 h}\right). \tag{B28d}$$

In the deep-water limit, $\beta \to 2\nu k_0^2/(d\omega_0/dk_0)$. In Fig. 16 we show the spatial damping coefficient β as a function of frequency for water with depth $h = 1.5$ mm.

APPENDIX C:
GREEN's FUNCTIONS AND POWER SPECTRA

We would like to find the power spectrum for a general driven dissipative linear equation

$$\mathcal{L}\varphi(\mathbf{x},t) = f(\mathbf{x},t) \tag{C1}$$

where $\mathcal{L}$ is a linear operator and $f(\mathbf{x},t)$ is a source term. We proceed by defining the Green's function in the usual way i.e., $\mathcal{L}G(\mathbf{x},\mathbf{x}',t,t') = \delta(\mathbf{x}-\mathbf{x}')\delta(t-t')$, in terms of which the solution to Eq. (C1) is
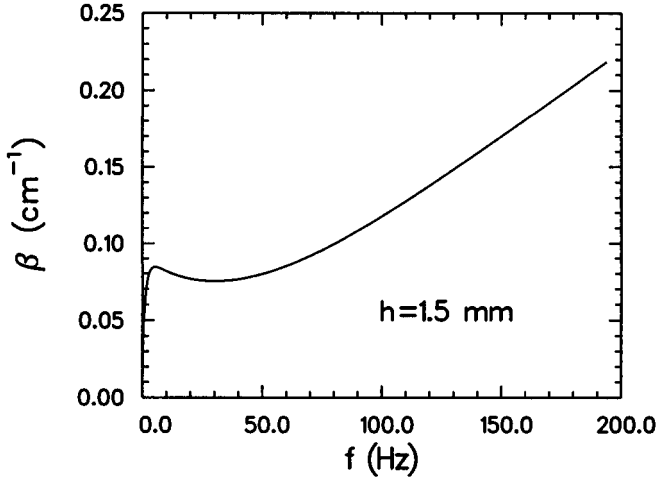
FIG. 16. The spatial damping coefficient as a function of frequency for water.

$$\varphi(\mathbf{x},t) = \int G(\mathbf{x},\mathbf{x}',t,t')f(\mathbf{x}',t')d^d x' dt'. \quad \text{(C2)}$$

If we consider the partial transform $\widetilde{\varphi}(\mathbf{x},\omega) = \int \varphi(\mathbf{x},t)e^{i\omega t}dt$, then we can write Eq. (C2) as

$$\widetilde{\varphi}(\mathbf{x},\omega) = \int \widetilde{G}(\mathbf{x},\mathbf{x}',\omega)\widetilde{f}(\mathbf{x}',\omega)d^d x'. \quad \text{(C3)}$$

The power spectrum is obtained by considering the ensemble average

$$\langle \widetilde{\varphi}(\mathbf{x},\omega)\widetilde{\varphi}^*(\mathbf{x}',\omega')\rangle = \int C(\mathbf{x},\mathbf{x}',t,t')e^{i\omega t}e^{-i\omega' t'}dt\, dt', \quad \text{(C4)}$$

where $C(\mathbf{x},\mathbf{x}',t,t') = \langle \varphi(\mathbf{x},t)\varphi(\mathbf{x}',t')\rangle$ is the correlation function. If the correlation function is time translationally invariant, i.e., $C(\mathbf{x},\mathbf{x}',t,t') = C(\mathbf{x},\mathbf{x}',t-t')$, then

$$\langle \widetilde{\varphi}(\mathbf{x},\omega)\widetilde{\varphi}^*(\mathbf{x}',\omega')\rangle = 2\pi S(\mathbf{x},\mathbf{x}',\omega)\delta(\omega-\omega'), \quad \text{(C5)}$$

where $S(\mathbf{x},\mathbf{x}',\omega) = \int C(\mathbf{x},\mathbf{x}',\tau)e^{i\omega\tau}d\tau$ is the power spectrum.

If we now substitute Eq. (C3) into Eq. (C4), we find that

$$\langle \widetilde{\varphi}(\mathbf{x}_1,\omega)\widetilde{\varphi}^*(\mathbf{x}_2,\omega')\rangle = \int \widetilde{G}(\mathbf{x}_1,\mathbf{x}',\omega)\widetilde{G}^*(\mathbf{x}_2,\mathbf{x}'',\omega')$$
$$\times \langle \widetilde{f}(\mathbf{x}',\omega)\widetilde{f}^*(\mathbf{x}'',\omega')\rangle d^d x' d^d x'', \quad \text{(C6)}$$

which using Eq. (C5) can be written as

$$S(\mathbf{x}_1,\mathbf{x}_2,\omega) = \int \widetilde{G}(\mathbf{x}_1,\mathbf{x}',\omega)\widetilde{G}^*(\mathbf{x}_2,\mathbf{x}'',\omega)S_f(\mathbf{x}',\mathbf{x}'',\omega)$$
$$\times d^d x' d^d x'', \quad \text{(C7)}$$

where $S_f(\mathbf{x},\mathbf{x}',\omega)$ is the power spectrum of the source term $f(\mathbf{x},t)$ defined in the same manner as Eq. (C5) [19].

Now let us suppose that the source term is spatially uncorrelated, and that its spectrum is independent of position. Then we can write $S_f(\mathbf{x},\mathbf{x}',\omega) = S_f(\omega)\rho(\mathbf{x})\delta(\mathbf{x}-\mathbf{x}')$, where $\rho(\mathbf{x})$ is the spatial density of the source [20]. Equation (C7) then becomes

$$S(\mathbf{x}_1,\mathbf{x}_2,\omega) = S_f(\omega)\int \widetilde{G}(\mathbf{x}_1,\mathbf{x}',\omega)\widetilde{G}^*(\mathbf{x}_2,\mathbf{x}',\omega)\rho(\mathbf{x}')d^d x'. \quad \text{(C8)}$$

Generally, the power spectrum is measured at a single point, in which case $\mathbf{x}_1 = \mathbf{x}_2 = \mathbf{x}$, and so

$$S(\mathbf{x},\omega) = S_f(\omega)\int |\widetilde{G}(\mathbf{x},\mathbf{x}',\omega)|^2\rho(\mathbf{x}')d^d x'. \quad \text{(C9)}$$

We will consider now only free-wave solutions where $\mathcal{L}$ has plane-wave eigenfunctions, i.e., $\mathcal{L}e^{i(\mathbf{q}\cdot\mathbf{x}-\omega t)} = D(\mathbf{q},\omega)e^{i(\mathbf{q}\cdot\mathbf{x}-\omega t)}$, where the eigenvalue $D(\mathbf{q},\omega)$ is the dispersion function, and $D(\mathbf{q},\omega)=0$ gives the dispersion relation. This case includes the linearized Navier-Stokes equations described in Appendix B, where the field $\varphi(\mathbf{x},t)$ represented the displacement of the free surface from equilibrium. The Green's function is then given by

$$\widetilde{G}_0(\mathbf{x},\mathbf{x}',\omega) = \frac{1}{(2\pi)^d}\int \frac{e^{i\mathbf{q}\cdot(\mathbf{x}-\mathbf{x}')}}{D(\mathbf{q},\omega)}d^d q. \quad \text{(C10)}$$

Integral Eq. (C10) would appear to be difficult to compute for the dispersion relation found in Appendix B, but we shall now argue what form it is likely to take. Let us consider, for pedagogical reasons, the telegraph equation

$$\frac{1}{c^2}\frac{\partial^2\psi}{\partial t^2} + \gamma\frac{\partial\psi}{\partial t} - \nabla^2\psi = f(\mathbf{x},t). \quad \text{(C11)}$$

This is just the usual driven wave equation to which has been added a dissipative term with positive coefficient γ. The dispersion function (which is now isotropic) is easily found to be $D(q,\omega) = q^2 - k^2$ where $k^2 = \omega^2/c^2 + i\gamma\omega$. Thus, $D^{-1}(q,\omega)$ will have poles at $\pm k$, which will be in opposite quadrants of the complex plane. The integral Eq. (C10) can then be evaluated by contour integration such that only the pole at $+k$ is enclosed, corresponding to a single source of spatially decaying outgoing waves [21]. It is found that

$$\widetilde{G}_0(\mathbf{x},\mathbf{x}',\omega) = (i/2k)e^{ik|\mathbf{x}-\mathbf{x}'|} \quad (d=1), \quad \text{(C12a)}$$

$$\widetilde{G}_0(\mathbf{x},\mathbf{x}',\omega) = (i/4)H_0^{(1)}(k|\mathbf{x}-\mathbf{x}'|) \quad (d=2), \quad \text{(C12b)}$$

where $H_0^{(1)}(z)$ is a Hankel function of the first kind. We postulate that the dispersion relation found in Appendix B will yield a similar pole structure with the consequence that the general form of Eqs. (C12) will remain unchanged, i.e., $\widetilde{G}_0(\mathbf{x},\mathbf{x}',\omega) = g_0(k|\mathbf{x}-\mathbf{x}'|)$, where the function $g_0(z)$ will depend on the specific form of the dispersion function $D(q,\omega)$.

[1] M. Kurihara, Rep. Res. Inst. Fluid Eng. Kyusyu Imp. Univ. **3**, 11 (1946).

[2] I. Tani, J. Phys. Soc. Jpn. **4**, 212 (1949).

[3] E. J. Watson, J. Fluid Mech. **20**, 481 (1964).

[4] V. E. Nakoryakov, B. G. Pokusaev, and E. N. Troyan, Int. J. Heat Mass Transfer **21**, 1175 (1978).

[5] R. I. Bowles and F. T. Smith, J. Fluid Mech. **242**, 145 (1992).

[6] A. A. M. Khalifa and J. A. McCorquodale, J. Hydraulic Res. **30**, 149 (1992).

[7] R. P. Godwin, Am. J. Phys. **61**, 829 (1993).

[8] T. Bohr, P. Dimon, and V. Putkaradze, J. Fluid Mech. **254**, 635 (1993).

[9] R. G. Olsson and E. T. Turkdogan, Nature **211**, 813 (1966).

[10] S. Ishigai, S. Nakanishi, M. Mizuno, and T. Imamura, Bull. J.S.M.E. **20**, 85 (1977).

[11] A. D. D. Craik, R. C. Latham, M. J. Fawkes, and P. W. F. Gribbon, J. Fluid Mech. **112**, 347 (1981).

[12] S. Middleman (private communication).

[13] M. C. Gutzwiller, *Chaos in Classical and Quantum Mechanics* (Springer-Verlag, New York, 1990).

[14] S. C. Creagh and P. Dimon, Phys. Rev. E **55**, 5551 (1997).

[15] See, for example, J. D. Jackson, *Classical Electrodynamics* (Wiley, New York, 1975), Chap. 7.

[16] This derivation follows that given for deep-water gravity waves in L. D. Landau and E. M. Lifshitz, *Fluid Mechanics* (Pergamon, Oxford, 1987), p. 94.

[17] This result was obtained in somewhat different form by other authors. See J. N. Hunt, Houille Blanche **19**, 685 (1964); L. Montefusco, Acc. Naz. Lincei, Rend. Accad. Sc. Fis. Mat. Nat. Naples Ser. VIII **46**, 704 (1969); A. J. Willson, Pure Appl. Geophys. **83**, 9 (1970); P. H. LeBlond and F. Mainardi, Acta Mechanica **68**, 203 (1987).

[18] J. Lighthill, *Waves in Fluids* (Cambridge University Press, Cambridge, 1993), p. 231.

[19] A similar expression was obtained earlier by K. M. van Vliet, A. van der Ziel, and R. R. Schmidt, J. Appl. Phys. **51**, 2947 (1980).

[20] This statement implicitly makes certain assumptions concerning the conservative properties of the system. For example, if $\mathcal{L}$ is the operator for the diffusion equation, then it implies that the field φ is not strictly conserved. [See, for example, T. Hwa and M. Kardar, Phys. Rev. Lett. **62**, 1813 (1989).] For surface waves, however, the situation is more complicated, and although there is certainly a conservation law for the surface displacement of an incompressible fluid, this statement may still be valid.

[21] See, for example, P. M. Morse and H. Feshback, *Methods of Theoretical Physics* (McGraw-Hill, New York, 1953).